JACS
JOURNAL OF THE AMERICAN CHEMICAL SOCIETY
Article
pubs.acs.org/JACS

Direct Synthesis of Self-Assembled Ferrite/Carbon Hybrid Nanosheets for High Performance Lithium-Ion Battery Anodes

Byungchul Jang,[†,∥] Mihyun Park,[‡,∥] Oh B. Chae,[‡] Sangjin Park,[‡] Youngjin Kim,[‡] Seung M. Oh,[‡] Yuanzhe Piao,*[,†,§] and Taeghwan Hyeon*[,†,‡]

[†]Department of Nano Science and Technology, Graduate School of Convergence Science and Technology, Seoul National University, 864-1 Iui-dong, Yeongtong-gu, Suwon-si, Gyeonggi-do 443-270, South Korea

[‡]World Class University (WCU) program of Chemical Convergence for Energy & Environment (C2E2), and School of Chemical and Biological Engineering, Seoul National University, 599 Gwanangno, Gwanak-gu, Seoul 151-744, South Korea

[§]Advanced Institutes of Convergence Technology, 864-1 Iui-dong, Yeongtong-gu, Suwon-si, Gyeonggi-do 443-270, South Korea

Supporting Information

ABSTRACT: Extensive applications of rechargeable lithium-ion batteries (LIBs) to various portable electronic devices and hybrid electric vehicles result in the increasing demand for the development of electrode materials with improved electrochemical performance including high energy, power density, and excellent cyclability, while maintaining low production cost. Here, we present a direct synthesis of ferrite/carbon hybrid nanosheets for high performance lithium-ion battery anodes. Uniform-sized ferrite nanocrystals and carbon materials were synthesized simultaneously through a single heating procedure using metal−oleate complex as the precursors for both ferrite and carbon. 2-D nanostructures were obtained by using sodium sulfate salt powder as a sacrificial template. The 2-D ferrite/carbon nanocomposites exhibited excellent cycling stability and rate performance derived from 2-D nanostructural characteristics. The synthetic procedure is simple, inexpensive, and scalable for mass production, and the highly ordered 2-D structure of these nanocomposites has great potential for many future applications.

INTRODUCTION

Rapidly growing demand for energy storage devices for portable electronic devices and electric vehicles will require high performance rechargeable batteries. Among the various rechargeable batteries, the lithium-ion battery (LIB) has been most intensively used for its outstanding energy and power density performance.[1−3] Although LIBs have been widely used in a variety of applications, many issues including their energy density, durability, and economic efficiency are still being intensively studied for further improvement. In particular, the development of noble electrode materials with high energy density and cycling stability is one of the hottest topics in LIB research. Transition-metal oxides are promising high-energy-density materials with their high theoretical capacity (~1000 mAh g^{-1}), which considerably exceeds that of commercial graphitic anodes (372 mAh g^{-1}).[4,5] However, low electrical conductivity and poor durability have impeded their use as LIB electrode materials. During charging and discharging of transition-metal oxide anodes, reversible intercalation of Li ions between the lattices occurs through the so-called conversion reaction mechanism.[6] This process causes considerable volume change and reduced crystallinity of the anode material with prolonged cycling, degrading the anode performance.[7,8] Consequently, transition-metal oxide anode research has been focused on improving the charge transport and mechanical durability.

Nanostructured electrode materials have attracted great interest as a solution to the above-mentioned problems.[9−13] Their nanostructures can provide short path lengths for the transport of electrons and Li ions, resulting in the good conductivity and fast charge/discharge rates. Furthermore, these nanomaterials can withstand mechanical strain during Li ion insertion/desertion better than that of bulk materials. However, due to the high surface-to-volume ratio and high surface free energy of the nanomaterials, undesirable side reactions can occur easily on their surfaces, including electrolyte degradation. Many kinds of metal−oxide/carbon nanocomposites have been investigated to overcome these problems.[14−19] Coating a carbon layer on the surface of metal oxide nanoparticles can reduce the side reactions at the interface between metal oxide and electrolyte. Moreover, good electrical conductivity of carbon can complement the low conductivity of metal oxides. In recent years, several fabrication methods have been reported for metal−oxide/carbon nanocomposites. Heating mixtures of metal salt and carbon precursors has led to the formation of metal−oxide/carbon composites.[20,21] However, the products were usually poor quality in both uniformity and homogeneity of the composite structure.[20] Furthermore, the complicated synthetic process,[21] comprising

Received: June 8, 2012
Published: August 27, 2012

   dx.doi.org/10.1021/ja305539r | J. Am. Chem. Soc. 2012, 134, 15010−15015

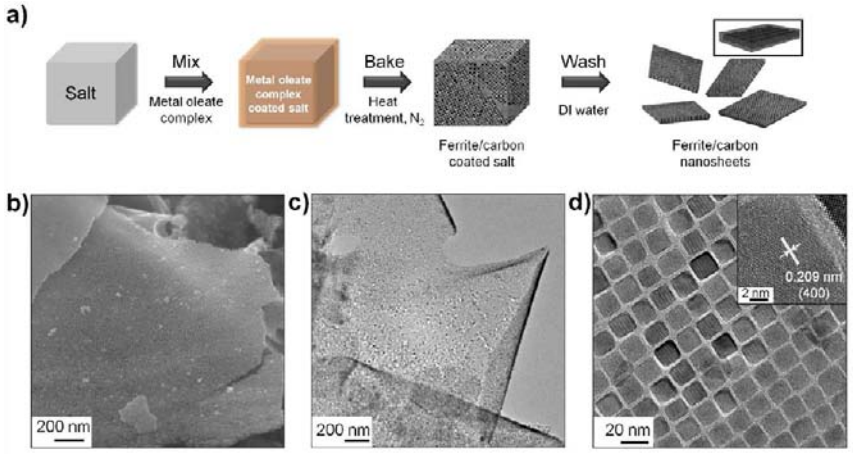

Figure 1. (a) Schematic representation of the preparation of ferrite/carbon nanosheets by salt-template process. (b) FESEM image and (c,d) TEM images of 16 nm iron−oxide/carbon nanosheets. The inset shows a HRTEM image demonstrating the highly crystalline nature of the nanosheets.

multiple reactions using autoclaves, lowers productivity as compared to other single-step processes. Consequently, new easy fabrication methods are required for metal−oxide/carbon nanocomposites. Very recently, the Archer group reported an in situ synthesis of nanoparticles embedded in a porous carbon matrix through a miniemulsion polymerization process, which exhibited stable electrochemical cycling performance.[22,23] We have developed a thermal treatment method, called as "wrap−bake−peel process," which can preserve the sizes and shapes of the nanocrystals during thermal treatment.[24]

The controlled assembly of uniform-sized nanocrystals has attracted great attention because well-aligned ensembles of inorganic nanocrystals often exhibit interesting collective properties that are different from those displayed by individual nanocrystals and bulk samples.[25−33] Various synthetic approaches[34−39] were developed for periodically ordered arrays of the synthesized nanoparticles including "evaporation-driven" methods[36,37] and "destabilization-driven" approaches.[38,39] However, as far as we know, there are no reports about synthesis and self-assembly processes simultaneously achieving a nanoparticle/carbon hybrid structure with long-range ordered arrays. Herein, we present a single-step method for the direct preparation of self-assembled ferrite/carbon hybrid nanosheets, and their applications to high performance lithium-ion battery anodes.

EXPERIMENTAL SECTION

Preparation of 16 nm Iron−Oxide/Carbon Hybrid Nanosheets. In a typical synthesis, 0.36 g of iron(III) chloride hexahydrate ($FeCl_3{\cdot}6H_2O$, 1.33 mmol, Aldrich, 98%) was dissolved in 1.0 mL of DI water and then mixed with 1.22 g of sodium oleate (4 mmol, TCI, 95%). The resulting mixture was aged at 85 °C for 3 h, and then was mixed with 10 g of sodium sulfate powder (Na_2SO_4, Aldrich, 98%). The mixture was heated to 600 °C at the heating rate of 10 °C min^{-1} under N_2 atmosphere and then kept at that temperature for 3 h. After being cooled, the product was washed with DI water and dried at 100 °C for 6 h.

Preparation of 30 nm Iron−Oxide/Carbon Nanosheets. In a typical synthesis, 0.36 g of iron(III) chloride hexahydrate ($FeCl_3{\cdot}6H_2O$, 1.33 mmol, Aldrich, 98%) was dissolved in 1.0 mL of DI water and then mixed with 1.22 g of sodium oleate (4 mmol, TCI, 95%). This mixture was aged at 85 °C for 3 h. The resulting material was mixed with 10 g of sodium sulfate powder (Na_2SO_4, Aldrich, 98%). The mixture was heated to 600 °C at the heating rate of 5 °C min^{-1} under N_2 atmosphere, and then kept at that temperature for 3 h. After being cooled, the product was washed with DI water and dried at 100 °C for 6 h.

Preparation of 3-D Nanocomposites. The procedure was the same as the preparation of ferrite/carbon hybrid nanosheets described above except that sodium sulfate powder was not added.

Preparation of 10 nm Manganese−Ferrite/Carbon Nanosheets. In a typical synthesis, 0.087 g of manganese(II) chloride tetrahydrate ($MnCl_2{\cdot}4H_2O$, 0.44 mmol, Aldrich, 98%) and 0.24 g of iron(III) chloride hexahydrate ($FeCl_3{\cdot}6H_2O$, 0.89 mmol, Aldrich, 98%) were dissolved in 1.0 mL of DI water and then mixed with 1.22 g of sodium oleate (4 mmol, TCI, 95%). This mixture was aged at 85 °C for 3 h. The subsequent heating and post-treatment procedures were the same as for iron−oxide/carbon nanosheets described above, except for the heating rate, which was 5 °C min^{-1}.

Characterization. Transmission electron microscopy (TEM) images were obtained using a JEOL EM-2100F microscope, and field-emission scanning electron microscopic (FESEM) images were obtained with a Hitachi S-4800 microscope. X-ray diffraction (XRD) analysis was carried out using a Rigaku Dmax 2500 diffractometer. Raman spectrum was obtained by using MonoRa500i. Electrical conductivity measurement was performed by using a CMT 100 MP four-point probe station.

For the preparation of electrodes, a dry powder of the nanocomposite (active material), super P (carbon additive), and poly(vinylidenefluoride) (binder) (85:5:10) were mixed and coated on a piece of copper foil (current collector). After the residual moisture was removed by drying in a vacuum oven at 120 °C for 12 h, the electrode plate was pressed to improve the interparticle contact and to reinforce adhesion between particles and the current collector. The electrochemical tests were performed by using a coin-type electrochemical cell (2032-type), which was fabricated with lithium foils as the counter and reference electrodes and 1.0 M $LiPF_6$ dissolved in a mixture of ethylene carbonate (EC) and dimethyl carbonate (DMC) (1:2 in vol. ratio) as the electrolyte. To cycle the coin-type electrochemical cells, they were discharged with a constant current of 100 mA g^{-1} to 0.05 V (vs Li/Li^+) and constant voltage at 0.05 V (vs Li/Li^+) to 50 mA g^{-1} and charged with a constant current of 100 mA g^{-1} to 3.0 V (vs Li/Li^+). In the rate capability test, the lithiation current density was fixed at 100 mA g^{-1}, but the delithiation current density was changed every five cycles according to this sequence of values: 100, 200, 500, 1000, 3000, and 5000 mA g^{-1}.

RESULTS AND DISCUSSION

The overall synthetic procedure is depicted in Figure 1a. In the direct synthesis of the ferrite/carbon hybrid nanosheets, we adopted two strategies. First, the surface of thermally stable salt particles was used as the template for the 2-D nanostructure.

dx.doi.org/10.1021/ja305539r | J. Am. Chem. Soc. 2012, 134, 15010−15015

Second, metal−oleate complex was used as the precursor of both ferrite[40−43] and carbon. Upon heating under inert atmosphere, the coating layer on the surface of the salt particles was converted to a carbon sheet of uniform thickness. In the synthesis, an aqueous solution of metal chloride and sodium oleate were mixed together, whereupon sodium sulfate was added and then ground mechanically until it became a fine powder. During this process, in situ formed metal−oleate complex was uniformly coated on the surface of sodium sulfate particles. This mixture was heated at ∼600 °C under inert atmosphere to form 2-D ferrite/carbon hybrid nanosheet structures. Finally, the hybrid nanosheets were separated by dissolving sodium sulfate particles in deionized (DI) water.

The morphology of the hybrid nanosheets was analyzed by scanning electron microscopy (SEM) and transmission electron microscopy (TEM). In Figure 1, it is shown that well-ordered uniform iron oxide nanocubes were embedded in a carbon sheet. The mean size and relative standard deviation of the nanocubes were measured to be 16 nm and 5.9%, respectively (16 nm iron−oxide/carbon nanosheets). Because of their size and shape uniformity, they were assembled in a highly ordered 2-D array that was evenly distributed across the carbon matrix, and each nanocrystal was perfectly concealed within a carbon layer, which was a few nanometers thick. The carbon sheet itself was very thin, and the surface profile of the carbon sheet reflects roughly the embedded array of nanocubes, as shown in the SEM image (Figure 1b). SEM analysis on as-prepared nanosheets before removing the salt powder revealed that they were actually formed on the surface of the salt particles (Figure S1 in the Supporting Information), which confirms the role of salt particles as the template for the 2-D structure. Furthermore, the dimensions of the 2-D nanocomposites were on the micrometer scale, which is roughly the same as the size of a flat surface of the salt particles. As shown in the inset of Figure 1d, the nanocubes were highly crystalline, and *d*-spacings of the lattice fringes indicate that the faces of the nanocubes are {100} planes of ferrite structure (Figure S2). The evolution of the cubic shape is attributed to the relative stabilization of the {100} face as compared to the {111} and {110} faces.[44]

The size and shape of the iron oxide nanocrystals were controlled by the heating rate and the temperature. When the heating rate was 5 °C min^{-1}, the size of the iron oxide nanocrystals was increased to ∼30 nm (30 nm iron−oxide/carbon nanosheets), and the shape became more spherical as compared to the 16 nm-sized nanocubes (Figure 2a,b). In general, when the heating rate was higher or lower than 10 °C min^{-1}, the size distribution of the nanocrystals became broadened with the mean size of >30 nm (Figures S3, S4). The size of the iron oxide nanocrystals was also affected by the heating temperature (Figure S5). According to TEM analysis, the formation of iron oxide nanocrystals was initiated at ∼250 °C. Considering that carbonization of organic precursors usually takes place at temperatures higher than 400 °C, it is likely that iron oxide nanocrystals were formed and assembled into a 2-D array as the temperature was increased from 250 to 400 °C, which is followed by the conversion of surfactant layer to carbon phase. The current synthetic process is easy to scale up, and when we ran the reaction using 13.3 mmol of iron oleate precursor, 1.3 g of the iron−oxide/carbon nanocomposite was obtained (Figure S6). The synthetic procedure for iron−oxide/carbon nanocomposite can be easily extended to other ferrites. Using a mixture of manganese(II) and iron(III) chloride, manganese−ferrite/carbon nanosheets were

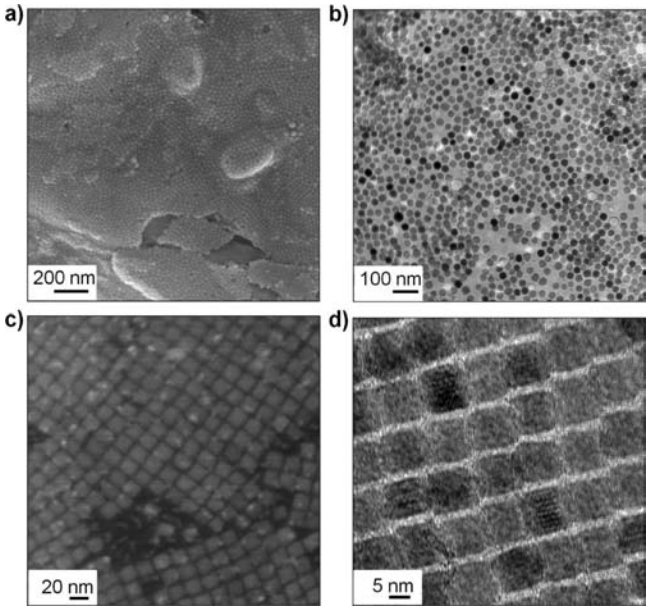

Figure 2. (a) FESEM image and (b) TEM image of 30 nm iron−oxide/carbon nanosheets, (c) FESEM image, and (d) TEM image of 10 nm manganese−ferrite/carbon nanosheets.

obtained through the optimized heating rate of 5 °C min^{-1}. As shown in Figure 2c, the 2-D array of manganese-ferrite/carbon nanosheets was as uniform as the array of 16 nm iron−oxide/carbon nanosheets in Figure 1, and the mean size of the manganese−ferrite nanocrystals was 10 nm (10 nm manganese−ferrite/carbon nanosheets). The composition of Mn and Fe in the nanocrystals was controlled by varying the ratio of manganese(II) chloride to iron(III) chloride added during the formation of metal−oleate complexes (Figure S7).

The crystal structures of the metal oxide nanocrystals in the nanocomposites were investigated by powder X-ray diffraction (XRD) measurement (Figure S8). The XRD patterns of the 16 and 30 nm-sized iron oxide nanocrystals in the composite matched well with the standard patterns of maghemite (γ-Fe_2O_3, JCPDS 39-1346) and magnetite (Fe_3O_4, JCPDS 85-1436), respectively. The size-dependent transition of iron oxide nanocrystals from γ-Fe_2O_3 to Fe_3O_4 has been reported previously.[28] The XRD pattern of manganese ferrite nanocrystals in the composite could be assigned to the standard of manganese ferrite ($MnFe_2O_4$, JCPDS 73-1964).

It is worth emphasizing here that the carbon nanostructure of our composite material is very unique. To observe its morphology in detail, we removed embedded iron oxide nanocubes via acid etching. When the ferrite/carbon nanosheets were refluxed in 2.5 M HNO_3 solution for 1 h, hollow 2-D carbon nanoframes were obtained. The 2-D nanofoam sheets were free-standing and well-dispersible in various solvents including ethanol and water. Interestingly, in the TEM images (Figure 3), the carbon nanostructure remained intact after etching, indicating its mechanical rigidity, and regularly spaced carbon networks extended continuously throughout the whole sheet.

Before investigating the electrochemical properties of the nanosheets, we prepared three-dimensional iron−oxide/carbon nanocomposites (3-D nanocomposites) for comparison with the ferrite/carbon nanosheets (Figure S9). The synthetic procedure was the same as that for the 30 nm iron−oxide/carbon nanosheets except that salt powder was not added

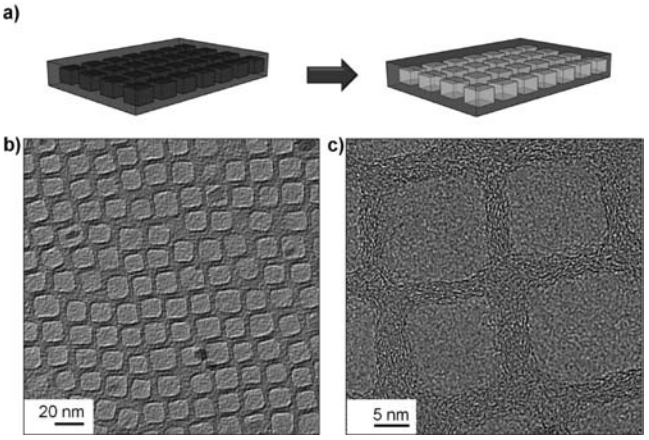

Figure 3. (a) Schematic representation of the preparation of the carbon nanofoams. (b,c) TEM images of carbon nanofoams after removal of 16 nm iron oxide nanocrystals from the nanosheets.

before the heat treatment. Without the template, carbon agglomerates embedded with spherical iron oxide nanocrystals with a diameter of ~40 nm were generated. The array of nanocrystals in the composite was less ordered than in the ferrite/carbon nanosheets due to the broad size distribution. The carbon contents (Table S1) of the 16 nm iron−oxide/carbon nanosheets, 30 nm iron−oxide/carbon nanosheets, and 3-D nanocomposites were 32−35, 44, and 25 wt %, respectively. To reduce carbon contents of the hybrid nanocomposites, we changed the precursor from iron(III) oleate to iron(III) carboxylates with shorter hydrocarbon chain length, that is, iron(III) caprylate and iron(III) laurate. However, these precursors were decomposed before the carbonization process, resulting in the irregular shaped nanoparticles without 2-D assembled structure (Figure S10, Table S2).

The characteristics of carbon in the nanosheets were characterized by electrical conductivity measurement and Raman spectroscopy. Electrical conductivity of the ferrite/carbon nanosheets was measured to be 4×10^{-3} S cm^{-1}. The Raman spectrum of the ferrite/carbon nanosheets showed two distinguishable peaks at around 1335 cm^{-1} (D band) and 1605 cm^{-1} (G band) with similar intensity (Figure S10), indicating that the obtained carbon materials were disordered nanocrystalline graphite.[45,46]

As a demonstration of the ferrite/carbon nanosheets as LIB anode materials, we carried out electrochemical tests in a coin type cell assembly. First, galvanostatic discharge/charge voltage profiles were obtained at a current density of 100 mA g^{-1} (Figure 4). In the first cycle, the profiles of the four electrodes, 16 nm iron−oxide/carbon nanosheets, 30 nm iron−oxide/carbon nanosheets, 10 nm manganese−ferrite/carbon nanosheets, and 3-D nanocomposites, appeared similar. Plateaus at about 1.6 and 0.8 V versus Li$^+$/Li in the lithiation and delithiation curves are a well-known signature of the conversion reactions of transition-metal oxides.[6] However, the specific capacity of each electrode evolved quite distinctly from the others in the subsequent 20 cycles. The capacities of all of the ferrite/carbon nanosheet electrodes stabilized after 10 cycles, while the capacity of the 3-D nanocomposite electrode faded rapidly. In Figure 5a, the delithiation capacities of the electrodes were plotted in terms of cycling number. In the plot, the delithiation capacities of the ferrite/carbon nanosheet electrodes were kept near or above 600 mAh g^{-1} after 50 cycles. On the other hand, the capacity of the 3-D composite electrode was reduced considerably to 323 mAh g^{-1}. These data clearly show the contribution of 2-D nanosheet morphology to capacity retention during cycling. The rate capability of the electrodes is also shown in Figure 5b. At a very high rate of 5000 mA g^{-1}, 81.5% of original capacity was retained for the manganese−-ferrite/carbon nanosheets, whereas 68.7%, 56.8%, and 41.6% were retained for 16 nm iron−oxide/carbon nanosheets, 30 nm iron−oxide/carbon nanosheets, and 3-D nanocomposites, respectively.

In electrochemical cycling of the ferrite/carbon nanocomposites, considerable change in the volume of metal oxide takes place due to the conversion reactions, which lower the integrity of the electrode structure and increase the internal resistance. It has been reported that the presence of carbon coating can reduce mechanical deformation by buffering the volume change of the active materials in the electrode.[47,48] Comparing the ferrite/carbon nanosheets and 3-D nanocomposites, well-ordered ferrite/carbon nanosheets have several advantages in terms of resistance to mechanical deformation. The self-assembled nanocrystal structure seems

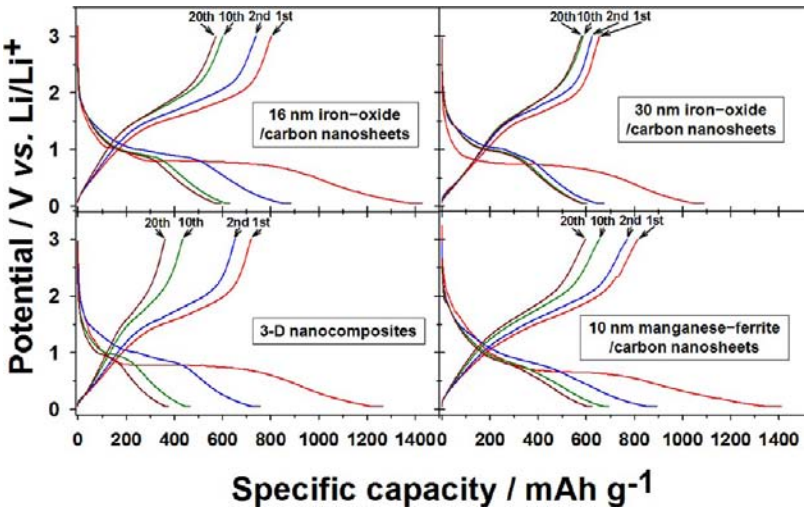

Figure 4. Galvanostatic discharge (lithiation, downward) and charge (delithiation, upward) voltage profiles.

dx.doi.org/10.1021/ja305539r | J. Am. Chem. Soc. 2012, 134, 15010−15015

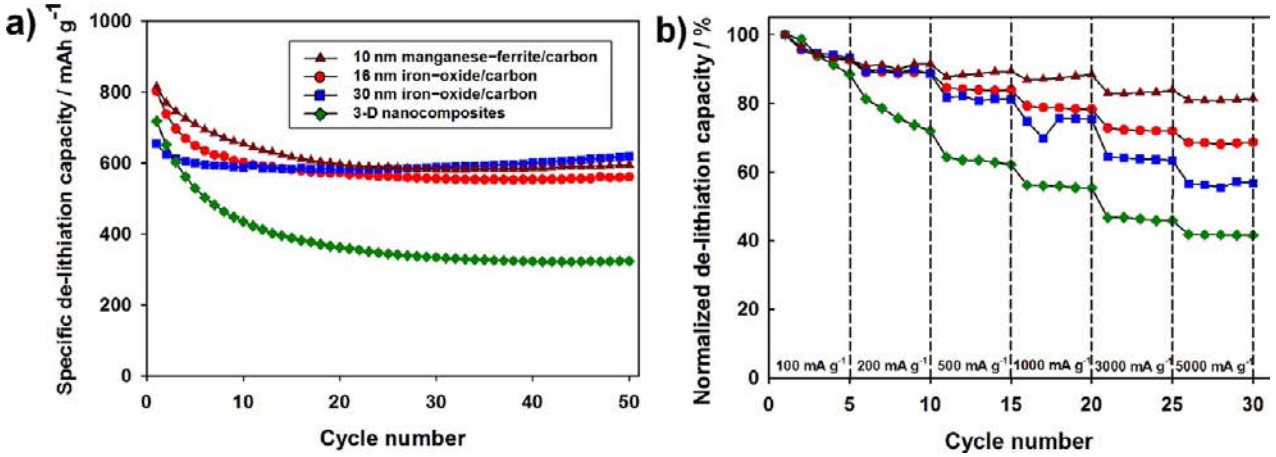

Figure 5. (a) Lithiation/delithiation capacities and (b) rate performance according to the cycle number of ferrite/carbon nanosheet electrodes.

to induce the regularly spaced carbon walls between the nanocrystals, providing high tensile strength in the vertical direction of the carbon sheet. In addition, ferrite/carbon nanosheets have more room to expand in this direction than 3-D nanocomposites, which can provide a buffer for the volume change of the nanocrystals. As a result, these structural factors can contribute to good cycle performance of the ferrite/carbon nanosheets, as shown in Figure 5a. To investigate the mechanical deformation of the ferrite/carbon nanosheets during the electrochemical cycling, TEM observations were made on the nanosheet electrodes after 10th charge/discharge cycling at a rate of 100 mA g^{-1} (Figure 6). The ferrite

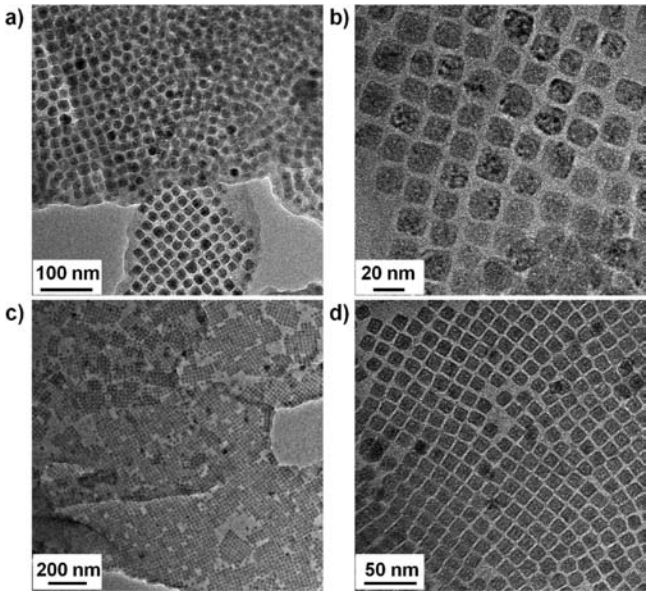

Figure 6. TEM images of (a,b) 16 nm iron–oxide/carbon nanosheets, and (c,d) 10 nm manganese–ferrite/carbon nanosheets after 10th charge/discharge cycling at a rate of 100 mA g^{-1}.

nanoparticles maintained the shape and size, and the assembled nanosheet structure was sustained without peeling off. The encapsulating carbon shells seem to help to maintain the structure of ferrite/carbon nanosheet electrodes. The rate capacity of the electrodes is affected by the diffusion of lithium ions from the electrolyte to the active material. In Figure 5b, the ferrite/carbon nanosheets show much better performance than the 3-D nanocomposite. This superior electrochemical performance of the ferrite/carbon nanosheets is due to their short diffusion path and large accessible surface for the effective insertion of lithium ions. Moreover, the size of the ferrite nanocrystals strongly affected the electrochemical performance at high charging/discharging rates. Smaller-sized ferrite nanocrystals were more efficient for fast diffusion process, and the Coulombic efficiency of the nanosheets seem to be less affected by the decomposition of electrolytes on the surface of electrodes because carbon shell protected the ferrite nanocrystals.[49] Furthermore, the large Coulombic capacity at high discharge rates seems to have resulted from the uniform-sized ferrite nanoparticles.[50]

■ CONCLUSIONS

In this study, two-dimensional nanostructures of ferrite/carbon composites were directly synthesized from metal–oleate precursor through a salt-template process. Uniform metal oxide nanocrystals and a supporting carbon layer were simultaneously synthesized from metal–oleate complex. When these ferrite/carbon nanosheets were employed as LIB anodes, the electrochemical performances showed outstanding enhancement of durability and rate performance as compared to the 3-D agglomerated nanocomposites. These synthetic procedures are not only easily scalable for mass production but also extensible to various 2-D inorganic-nanocrystal/carbon nanocomposites that can potentially be applied to practical energy storage and conversion devices.

■ ASSOCIATED CONTENT

Supporting Information

Additional SEM images, TEM images, XRD patterns, and Raman spectrum of ferrite/carbon nanosheets, size distributions of the iron oxide nanoparticles, a photograph showing large-scale synthesis, and elemental analysis results. This material is available free of charge via the Internet at http://pubs.acs.org.

■ AUTHOR INFORMATION

Corresponding Author

thyeon@snu.ac.kr; parkat9@snu.ac.kr

Author Contributions

[‖]These authors contributed equally.

Notes

The authors declare no competing financial interest.

■ ACKNOWLEDGMENTS

T.H. acknowledges financial support by the Korean Ministry of Education, Science and Technology through the Global Research Laboratory (2011-0021628), Strategic Research (2010-0029138), and the World Class University (R31-10013) programs of the National Research Foundation (NRF) of Korea. Y.P. would like to thank the Smart IT Convergence System Research Center funded by the Ministry of Education, Science and Technology as Global Frontier Project (0543-20110015) for financial support. This work was also supported by the grant from the Industrial Source Technology Development Program (10041041) of the Ministry of Knowledge Economy (MKE) of Korea.

■ REFERENCES

(1) Armand, M.; Tarascon, J.-M. *Nature* **2008**, *451*, 652.
(2) Kang, K.; Meng, Y. S.; Bréger, J.; Grey, C. P.; Ceder, G. *Science* **2006**, *311*, 9770.
(3) Ceder, G. *MRS Bull.* **2010**, *35*, 693.
(4) Behera, S. K. *J. Power Sources* **2011**, *196*, 8669.
(5) Ma, J.; Lian, J.; Duan, X.; Liu, X.; Zheng, W. *J. Phys. Chem. C* **2010**, *114*, 10671.
(6) Poizot, P.; Laruelle, S.; Grugeon, S.; Dupont, L.; Tarascon, J.-M. *Nature* **2000**, *407*, 496.
(7) Cabana, J.; Monconduit, L.; Larcher, D.; Palacín, M. R. *Adv. Mater.* **2010**, *22*, E170.
(8) Kim, M. G.; Cho, J. *Adv. Funct. Mater.* **2009**, *19*, 1497.
(9) Aricò, A. S.; Bruce, P. G.; Scrosati, B.; Tarascon, J.-M.; van Schalkwijk, W. *Nat. Mater.* **2005**, *4*, 366.
(10) Bruce, P. G.; Scrosati, B.; Tarascon, J.-M. *Angew. Chem., Int. Ed.* **2008**, *47*, 2930.
(11) Chan, C. K.; Peng, H.; Liu, G.; McIlwrath, K.; Zhang, X. F.; Huggins, R. A.; Cui, Y. *Nat. Nanotechnol.* **2008**, *3*, 31.
(12) Lou, X. W.; Deng, D.; Lee, J. Y.; Feng, J.; Archer, L. A. *Adv. Mater.* **2008**, *20*, 258.
(13) Wang, H.; Cui, L.-F.; Yang, Y.; Casalongue, H. S.; Robinson, J. T.; Liang, Y.; Cui, Y.; Dai, H. *J. Am. Chem. Soc.* **2010**, *132*, 13978.
(14) Hu, Y.-S.; Demir-Cakan, R.; Titirici, M.-M.; Müller, J.-O.; Schlögl, R.; Antonietti, M.; Maier, J. *Angew. Chem., Int. Ed.* **2008**, *47*, 1645.
(15) Kim, H.; Cho, J. *Nano Lett.* **2008**, *8*, 3688.
(16) Lou, X. W.; Li, C. M.; Archer, L. A. *Adv. Mater.* **2009**, *21*, 2536.
(17) Wu, X.-L.; Jiang, L.-Y.; Cao, F.-F.; Guo, Y.-G.; Wan, L.-J. *Adv. Mater.* **2009**, *21*, 2710.
(18) Piao, Y.; Kim, H. S.; Sung, Y.-E.; Hyeon, T. *Chem. Commun.* **2010**, *46*, 118.
(19) Ban, C.; Wu, Z.; Gillaspie, D. T.; Chen, L; Yan, Y.; Blackburn, J. L.; Dillon, A. C. *Adv. Mater.* **2010**, *22*, E145.
(20) Hang, B. T.; Watanabe, I.; Doi, T.; Okada, S.; Yamaki, J.-I. *J. Power Sources* **2006**, *161*, 1281.
(21) Zhang, W.-M.; Wu, X.-L.; Hu, J.-S.; Guo, Y.-G.; Wan, L.-J. *Adv. Funct. Mater.* **2008**, *18*, 3941.
(22) Yang, Z.; Shen, J.; Jayaprakash, N.; Archer, L. A. *Energy Environ. Sci.* **2012**, *5*, 7025.
(23) Yang, Z.; Shen, J.; Archer, L. A. *J. Mater. Chem.* **2011**, *21*, 11092.
(24) Piao, Y.; Kim, J.; Na, H. B.; Kim, D.; Baek, J. S.; Ko, M. K.; Lee, J. H.; Shokouhimehr, M.; Hyeon, T. *Nat. Mater.* **2008**, *7*, 242.
(25) Mann, S. *Nat. Mater.* **2009**, *8*, 781.
(26) Podsiadlo, P.; Krylova, G.; Lee, B.; Critchley, K.; Gosztola, D. J.; Talapin, D. V.; Ashby, P. D.; Shevchenko, E. V. *J. Am. Chem. Soc.* **2010**, *132*, 8953.
(27) Nie, Z.; Petukhova, A.; Kumacheva, E. *Nat. Nanotechnol.* **2010**, *5*, 15.
(28) Shevchenko, E. V.; Ringler, M.; Schwemer, A.; Talapin, D. V.; Klar, T. A.; Rogach, A. L.; Feldmann, J.; Alivisatos, A. P. *J. Am. Chem. Soc.* **2008**, *130*, 3274.
(29) Sun, S.; Murray, C. B.; Weller, D.; Folks, L.; Moser, A. *Science* **2000**, *287*, 1989.
(30) Talapin, D. V.; Shevchenko, E. V.; Bodnarchuk, M. I.; Ye, X.; Chen, J.; Murray, C. B. *Nature* **2009**, *461*, 964.
(31) Li, F.; Josephson, D. P.; Stein, A. *Angew. Chem., Int. Ed.* **2011**, *50*, 360.
(32) Nagaoka, Y.; Chen, O.; Wang, Z.; Cao, Y. C. *J. Am. Chem. Soc.* **2012**, *134*, 2868.
(33) Bodnarchuk, M. I.; Kovalenko, M. V.; Heiss, W.; Talapin, D. V. *J. Am. Chem. Soc.* **2010**, *132*, 11967.
(34) Dong, A.; Chen, J.; Vora, P. M.; Kikkawa, J. M.; Murray, C. B. *Nature* **2010**, *466*, 474.
(35) Dong, A.; Ye, X.; Chen, J.; Murray, C. B. *Nano Lett.* **2011**, *11*, 1804.
(36) Shevchenko, E. V.; Talapin, D. V.; Kotov, N. A.; O'Brien, S.; Murray, C. B. *Nature* **2006**, *439*, 55.
(37) Bodnarchuk, M. I.; Shevchenko, E. V.; Talapin, D. V. *J. Am. Chem. Soc.* **2011**, *133*, 20837.
(38) Rupich, S. M.; Shevchenko, E. V.; Bodnarchuk, M. I.; Lee, B.; Talapin, D. V. *J. Am. Chem. Soc.* **2009**, *132*, 289.
(39) Shevchenko, E. V.; Talapin, D. V.; Rogach, A. L.; Kornowski, A.; Haase, M.; Weller, H. *J. Am. Chem. Soc.* **2002**, *124*, 11480.
(40) Park, J.; An, K.; Hwang, Y.; Park, J.-G.; Noh, H.-J.; Kim, J.-Y.; Park, J.-H.; Hwang, N.-M.; Hyeon, T. *Nat. Mater.* **2004**, *3*, 891.
(41) Kwon, S. G.; Piao, Y.; Park, J.; Angappane, S.; Jo, Y.; Hwang, N.-M.; Park, J.-G.; Hyeon, T. *J. Am. Chem. Soc.* **2007**, *129*, 12571.
(42) Zeng, H.; Rice, P. M.; Wang, S. X.; Sun, S. *J. Am. Chem. Soc.* **2004**, *126*, 11458.
(43) Yu, W. W.; Falkner, J. C.; Yavuz, C. T.; Colvin, V. L. *Chem. Commun.* **2004**, 2306.
(44) Cheon, J.; Kang, N.-J.; Lee, S.-M.; Lee, J.-H.; Yoon, J.-H.; Oh, S. J. *J. Am. Chem. Soc.* **2004**, *126*, 1950.
(45) Ferrari, A. C.; Robertson, J. *Phys. Rev. B* **2000**, *61*, 14095.
(46) Sadezkya, A.; Muckenhuberb, H.; Grotheb, H.; Niessnera, R.; Pöschl, U. *Carbon* **2005**, *43*, 1731.
(47) Kim, J.; Chung, M. K.; Ka, B. H.; Ku, J. H.; Park, S.; Ryu, J.; Oh, S. M. *J. Electrochem. Soc.* **2010**, *157*, A412.
(48) Zhu, X.; Zhu, Y.; Murali, S.; Stoller, M. D.; Ruoff, R. S. *ACS Nano* **2011**, *5*, 3333.
(49) Lee, K. T.; Cho, J. *Nano Today* **2011**, *6*, 28.
(50) Darling, R.; Newman, J. *J. Electrochem. Soc.* **1997**, *144*, 4201.